

MATERIALS SCIENCE

Above-ordering-temperature large anomalous Hall effect in a triangular-lattice magnetic semiconductor

Masaki Uchida^{1,2,3*}, Shin Sato², Hiroaki Ishizuka¹, Ryosuke Kurihara^{4,5}, Taro Nakajima⁴, Yusuke Nakazawa², Mizuki Ohno^{1,2}, Markus Kriener⁵, Atsushi Miyake⁴, Kazuki Ohishi⁶, Toshiaki Morikawa⁶, Mohammad Saeed Bahramy², Taka-hisa Arima^{5,7}, Masashi Tokunaga^{4,5}, Naoto Nagaosa^{2,5}, Masashi Kawasaki^{2,5}

While anomalous Hall effect (AHE) has been extensively studied in the past, efforts for realizing large Hall response have been mainly limited within intrinsic mechanism. Lately, however, a theory of extrinsic mechanism has predicted that magnetic scattering by spin cluster can induce large AHE even above magnetic ordering temperature, particularly in magnetic semiconductors with low carrier density, strong exchange coupling, and finite spin chirality. Here, we find out a new magnetic semiconductor EuAs, where Eu²⁺ ions with large magnetic moments form distorted triangular lattice. In addition to colossal magnetoresistance, EuAs exhibits large AHE with an anomalous Hall angle of 0.13 at temperatures far above antiferromagnetic ordering. As also demonstrated by model calculations, observed AHE can be explained by the spin cluster scattering in a hopping regime. Our findings shed light on magnetic semiconductors hosting topological spin textures, developing a field targeting diluted carriers strongly coupled to noncoplanar spin structures.

INTRODUCTION

The anomalous Hall effect (AHE) is one of the most fundamental phenomena in magnetic conductors (1). In ferromagnets, the mechanisms of AHE are roughly classified into two groups: intrinsic mechanism related to the Berry curvature (2) and extrinsic mechanism by asymmetric scattering (3, 4). The intrinsic mechanism is related to the Berry curvature of electronic bands, which appears as a consequence of spin-orbit interaction. A similar effect also occurs from spin Berry phase (5, 6), in which case the Hall effect is related to the scalar spin chirality $\mathbf{S}_i \cdot (\mathbf{S}_j \times \mathbf{S}_k)$ of adjacent three spins; a related theory shows that the Hall conductivity is proportional to the scalar spin chirality in the weak coupling limit in dirty conductors (7). Large Hall current is produced by the intrinsic mechanism especially in the metallic conduction regime, and thus, it has been extensively studied for many years (8–11). In recent years, large Hall angles exceeding 0.1 have been found in a variety of magnetic topological semimetals, which host topological singularities of the Berry curvature in momentum space (12–18).

In contrast to the intrinsic mechanism, asymmetric scattering coupled with spin-orbit interaction is treated as small perturbation in the extrinsic mechanism, resulting in relatively small anomalous Hall angles of $10^{-2} \sim 10^{-3}$. Lately, however, it has been theoretically proposed that large AHE is induced by skew scattering by multiple spins with finite spin chirality (19, 20). In this mechanism,

anomalous Hall angles, roughly two orders of magnitude larger than in the case of single-spin scatterers, have been theoretically derived, especially in the limit of strong coupling between charge carriers and localized spins (20). Furthermore, this AHE can emerge even above the magnetic ordering temperature reflecting thermal average of the spin chirality, while the intrinsic AHE based on the Berry phase disappears above the ordering temperature. Actually, AHE above the magnetic ordering temperature has been observed in a metal hosting skyrmions (21, 22), which has been ascribed to the skew scattering by fluctuating but locally correlated spins originally forming the skyrmion lattice below the ordering temperature. Moreover, large AHE ascribed to the spin cluster scattering has been observed in a Kagome metal even without magnetic ordering (23). In this theory (20), on the other hand, it turns out that anomalous Hall angles rapidly increase with decrease in charge carriers and also with increase in its exchange coupling to localized spins. In addition, quantization of AHE can also be expected, once the low-density charge carrier corresponds to a topological spin configuration one by one (24, 25). Therefore, for realizing large Hall response by this mechanism, it is desirable to design magnetic conductors with more diluted carriers and stronger exchange coupling, while the study of AHE in the hopping conduction regime has been limited to conventional magnetic semiconductors so far (26–28).

Here, we take note of a novel magnetic semiconductor EuAs. Regarding this compound, only its crystal structure has been reported in the 1970s (29–31). As illustrated in Fig. 1A, EuAs has a unique hexagonal structure (Na₂O₂ type, space group: $P\bar{6}2m$) (30, 31), where Eu forms a distorted triangular lattice with geometrical frustration, different from other europium monochalcogenides and rare earth monopnictides with cubic structure (32, 33). Here, we report colossal magnetoresistance (CMR) and nonmonotonic AHE with large Hall angles observed even far above the Néel temperature. As also demonstrated by theoretical calculations, this large AHE can be explained by spin cluster skew scattering in the hopping regime.

¹Department of Physics, Tokyo Institute of Technology, Tokyo 152-8550, Japan.

²Department of Applied Physics and Quantum-Phase Electronics Center (QPEC), The University of Tokyo, Tokyo 113-8656, Japan. ³PRESTO, Japan Science and Technology Agency (JST), Chiyoda-ku, Tokyo 102-0075, Japan. ⁴Institute for Solid State Physics, The University of Tokyo, Kashiwa 277-8581, Japan. ⁵RIKEN Center for Emergent Matter Science (CEMS), Wako 351-0198, Japan. ⁶Neutron Science and Technology Center, Comprehensive Research Organization for Science and Society (CROSS), Tokai 319-1106, Japan. ⁷Department of Advanced Materials Science, University of Tokyo, Kashiwa 277-8561, Japan.

*Corresponding author. Email: m.uchida@phys.titech.ac.jp

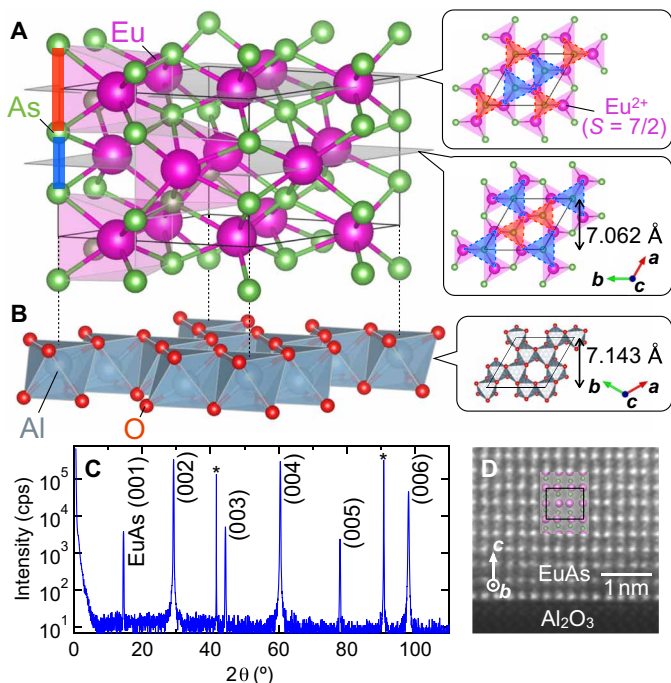


Fig. 1. Epitaxial stabilization of EuAs. (A) EuAs crystal structure and top views of alternately stacked Eu layers, where an Eu atom is located at the center of EuAs_6 triangular prisms. Reflecting short (blue) and long (red) As–As bonds along the c axis, distorted Eu triangular lattices composed of large (blue) and small (red) regular triangles are formed on the alternately stacked layers, as shown in the insets. (B) Al_2O_3 substrate crystal structure and top view of a surface layer. A rhombus corresponding to the EuAs unit cell represents the in-plane epitaxial relation. cps, counts per second. (C) X-ray diffraction $\theta - 2\theta$ scan of a single-crystalline EuAs film grown on the Al_2O_3 (0001) substrate. Substrate peaks are marked with an asterisk. (D) Cross-sectional high-angle annular dark field (HAADF)–scanning transmission electron microscopy STEM image of the EuAs film grown from the atomically sharp heterointerface. A side view of the EuAs crystal structure is also overlaid.

RESULTS

Structural characterization of EuAs films

Single-crystalline EuAs films were grown on lattice-matched Al_2O_3 substrates by molecular beam epitaxy. As shown in Fig. 1 (A and B), an Eu atom is located at the center of EuAs_6 triangular prisms, which are alternately stacked along the c axis. A dimer expressed by $[\text{As}-\text{As}]^{4-}$ is formed with short As–As bonds as in isostructural SrAs (30, 31), and thus, Eu is expected to be divalent (Eu^{2+} , $S = 7/2$). Corresponding to this dimerization, the Eu triangular lattice is distorted and composed of two large (blue) and small (red) regular triangles, as shown in Fig. 1A (insets) (see also fig. S4). X-ray diffraction $\theta - 2\theta$ scan in Fig. 1C shows sharp peaks from the EuAs {001} planes without any impurity ones. As confirmed in atomically resolved scanning transmission electron microscopy image in Fig. 1D, the EuAs film is epitaxially grown with forming a sharp heterointerface to the Al_2O_3 substrate. Further structural characterization was performed for examining the in-plane epitaxial relation and the Eu valence (Eu^{2+}) state (see note S1).

Colossal magnetoresistance

Figure 2 summarizes fundamental transport and magnetic properties of EuAs films. Longitudinal resistivity in Fig. 2A exhibits a

semiconducting temperature dependence with a kink at $T_N = 23.0$ K, which is interpreted as an antiferromagnetic (AFM) phase transition as detailed below. With applying the magnetic field, the resistivity markedly decreases by several orders of magnitude at the lowest temperature. This large negative magnetoresistance, which can be called CMR, appears even at far higher temperatures than T_N . CMR is confirmed also in the field sweep shown in Fig. 2B, where the drop of the resistivity at 1.4 K suddenly stops at $B_s = 14.5$ T. Magnetization in Fig. 2C saturates at the same field, exhibiting a transition to the forced ferromagnetic (FM) phase with a full magnetic moment of about $7\mu_B$. While temperature dependence of both the out-of-plane and in-plane magnetizations shows a sharp kink at T_N , the in-plane one is largely suppressed below T_N compared to the out-of-plane one, suggesting that Eu^{2+} Heisenberg spins are antiferromagnetically ordered on the a - b triangular lattice plane.

Looking at the magnetic structures more closely, neutron diffraction experiments were also performed for a EuAs film. As shown in Fig. 2D, magnetic reflections indexed by wave vectors of $\mathbf{q} = (1/2, 1/2, 0)$ and its equivalents were observed on the $(H, K, 0)$ plane, which indicates AFM spin correlation on the triangular lattice plane. Temperature dependence of these reflections was measured using a polarized neutron beam as shown in Fig. 2E. The neutron spin polarization at the sample position was set parallel to the c axis, and so, non-spin-flip (NSF) and spin-flip (SF) scattering intensities are proportional to squares of Fourier-transformed spin components parallel to the c axis and q vector, respectively. We found that the magnetic scattering below T_N is dominated by the SF scattering, indicating that the magnetic moments are confined in the triangular lattice planes. A minimal model to explain the present results is a collinear AFM order, in which magnetic moments are pointing perpendicular to both the c axis and q vector. However, taking into account the symmetry of the crystal structure, it should be allowed to have spin components parallel to the q vector, which leads to a noncollinear spin arrangement on the triangular lattice plane. Consideration of Dzyaloshinskii-Moriya interaction, whose vector points along the c axis for adjacent Eu spins on the triangular lattice plane, also leads the same consequence. The obtained magnetic phase diagram of EuAs is presented in Fig. 2F. With increasing the out-of-plane magnetic field, the coplanar spin configuration suggested by the neutron scattering experiment is expected to be transformed into a noncoplanar one by canting and then eventually into the fully polarized one.

It is naturally understood that CMR observed in the magnetic semiconductor EuAs is caused by diluted carriers coupled with the Eu^{2+} localized spins over a wide range of temperatures. In the double exchange model for strong coupling between charge carriers and localized spins, the transfer integral t for hopping carriers is expressed by $t \propto \cos(\theta/2)$ with the angle θ between adjacent localized spins (34, 35), explaining metallic conduction in the spin polarized state. In simple FM systems such as $\text{La}_{1-x}\text{Sr}_x\text{MnO}_3$ (36–38) and EuO (39), fluctuating spins near the FM transition are forcedly polarized by the applied magnetic field, and thus, CMR appears mainly above the Curie temperature. In the present case of AFM systems, on the other hand, CMR appears also below T_N as observed in NaCr_2O_4 (40) and EuTe (41), because antiferromagnetically ordered spins are gradually polarized by the applied magnetic field. In EuAs, CMR begins to emerge at temperatures far above T_N , suggesting that the in-plane AFM spin fluctuation evolves from such high temperatures on the frustrated triangular lattice.

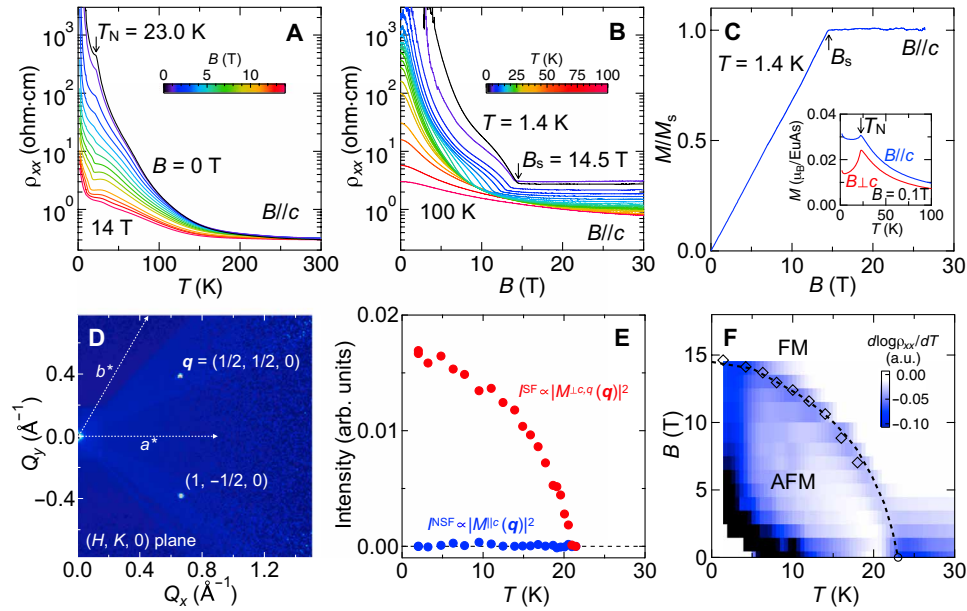


Fig. 2. New magnetic semiconductor EuAs. (A) Temperature dependence of longitudinal resistivity ρ_{xx} in EuAs, measured under various out-of-plane magnetic fields ($B \parallel c$). (B) Magnetic field sweep of ρ_{xx} at different temperatures. (C) Magnetization curve taken at the base temperature of 1.4 K. Saturation magnetization M_s is estimated at about $7\mu_B/\text{EuAs}$, considering volume of the EuAs film. Inset: Temperature dependence of magnetization for $B \parallel c$ and $B \perp c$ after zero field cooling. (D) Neutron diffraction pattern measured on the $(H, K, 0)$ plane at 3 K. (E) Temperature dependence of $q = (1/2, 1/2, 0)$ reflection peak, taken for spin-flip (SF) and non-spin-flip (NSF) scattering processes using a polarized neutron beam. (F) Magnetic phase diagram of EuAs for $B \parallel c$. A circle and a diamond represent the Néel temperature T_N and the saturation field B_s determined from the sweeps in (A) and (B). a.u., arbitrary units.

Anomalous hall signal above Néel temperature

In addition to CMR, EuAs exhibits unconventionally large AHE for a magnetic semiconductor. As shown in Fig. 3, Hall resistivity is almost proportional to B at 300 K, but a hump starts to appear at about 15 T, and it significantly increases with lowering temperature. It shows a maximum approximately at 70 K, a temperature far higher than T_N . With further lowering temperature toward T_N , the hump shifts to lower fields, and then below T_N , the hump is partially seen in the canted AFM phase below B_s and the Hall resistivity above B_s becomes almost proportional to B again. Apparently, this nonmonotonic Hall signal is not proportional to the field induced magnetization (M) as represented by the Brillouin function. In addition, the M -proportional component, estimated by linear extrapolation of the forced FM phase (10 K) data to zero field, is negligibly small. As seen in the above temperature and field dependences, this anomalous Hall signal is enhanced in the region where the Eu^{2+} spins on the triangular lattice are forcedly canted but not yet fully polarized. This implies that the observed AHE is mainly caused by noncoplanar spin texture or local fluctuations with finite spin chirality under the out-of-plane magnetic field.

The M -nonproportional anomalous Hall component is extracted using the following equation

$$\sigma_{yx} = \sigma_{\text{OHE}} + \sigma_{\text{AHE},M} + \sigma_{\text{AHE},\text{non}M} \quad (1)$$

with ordinary Hall conductivity σ_{OHE} , M -proportional anomalous Hall conductivity $\sigma_{\text{AHE},M}$, and M -nonproportional anomalous Hall conductivity $\sigma_{\text{AHE},\text{non}M}$. σ_{yx} is obtained by inverting the ρ_{xx} and ρ_{yx} matrix, and $\sigma_{\text{AHE},\text{non}M}$ can be estimated by subtracting σ_{OHE} and $\sigma_{\text{AHE},M}$ defined by

$$\sigma_{\text{OHE}} = \frac{-\frac{1}{pe}B}{\rho_{xx}^2 + \left(\frac{1}{pe}B\right)^2} \quad (2)$$

and

$$\sigma_{\text{AHE},M} = -A\sigma_{xx}^\alpha M \quad (3)$$

from the total Hall conductivity (for details, see the Supplementary Materials). Here, p denotes the hole carrier density, A denotes a constant independent of magnetic field and temperature, and α denotes a scaling factor relating σ_{xx} and $\sigma_{\text{AHE},M}$ (28). $\sigma_{\text{AHE},M}$ is calculated using $\alpha = 1.6$ and A determined in the forced FM phase at 10 K, and σ_{OHE} is determined on the assumption that it is the only contribution to the remaining component at 56 T (see also note S2). As confirmed in the Hall resistivity components converted from σ_{OHE} , $\sigma_{\text{AHE},M}$, and $\sigma_{\text{AHE},\text{non}M}$, the M -nonproportional component is more dominant than the M -proportional one. Although the spin fluctuation may not be fully suppressed and $\sigma_{\text{AHE},\text{non}M}$ may still slightly contribute at a high field of 56 T, this assumption gives the most conservative estimate of $\sigma_{\text{AHE},\text{non}M}$. The carrier density obtained from σ_{OHE} is nearly constant with temperature at $p \sim 3 \times 10^{17} \text{ cm}^{-3}$ (see fig. S6). It is also confirmed that the nonmonotonic Hall signal cannot be explained by a multicarrier model (see fig. S7).

AHE in the hopping regime

Figure 4A maps $\rho_{\text{AHE},\text{non}M}$ on the magnetic field–temperature phase diagram. $\rho_{\text{AHE},\text{non}M}$ remains over a wide high-temperature region spread from the AFM critical point, where the Eu^{2+} spins on the triangular lattice are expected to form local noncoplanar spin

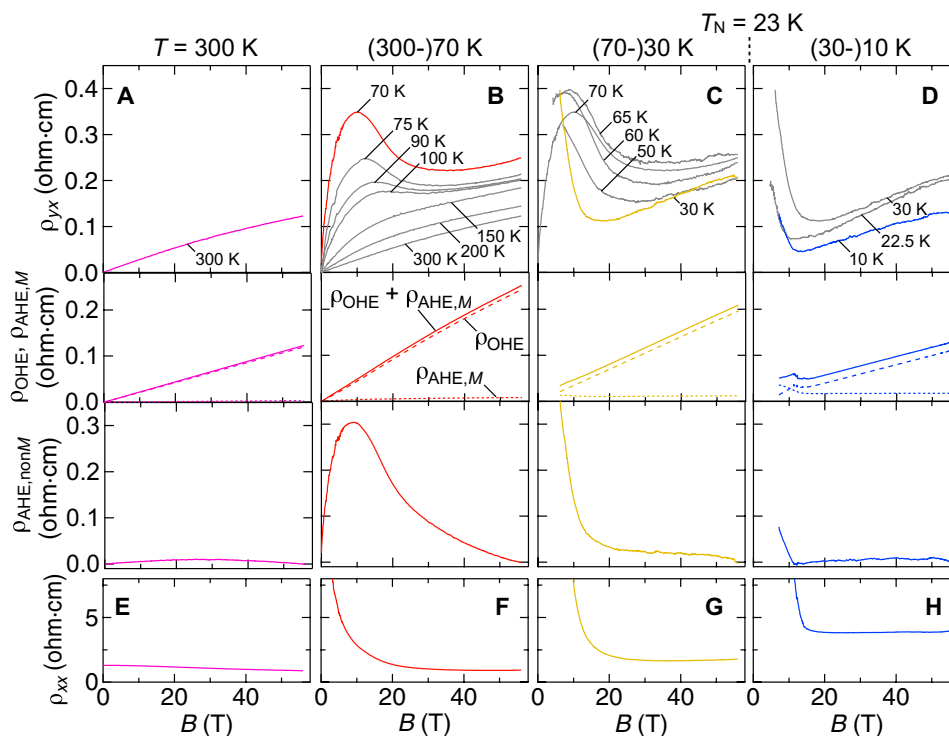


Fig. 3. Anomalous Hall resistivity observed above T_N . (A) Hall resistivity ρ_{yx} measured at 300 K and its separation into ordinary Hall resistivity ρ_{OHE} , M -proportional anomalous Hall resistivity $\rho_{AHE,M}$, and M -nonproportional anomalous Hall resistivity $\rho_{AHE,nonM}$. At this temperature, ρ_{yx} corresponds almost to the ordinary component. (B to D) Change of ρ_{yx} with decrease in temperature and its possible separation into ρ_{OHE} , $\rho_{AHE,M}$, and $\rho_{AHE,nonM}$ at 70, 30, and 10 K. Anomalous enhancement of $\rho_{AHE,nonM}$ can be confirmed from high temperatures well above T_N . (E to H) Magnetic field dependence of ρ_{xx} at the same temperatures.

structures or fluctuations with finite spin chirality. Despite the hopping conduction regime, anomalous Hall angle defined by $\rho_{AHE,nonM}/\rho_{xx}$ rises up to 0.13 at 70 K. This is a very large value for the extrinsic mechanism and also comparable to those recently achieved by the intrinsic mechanism (12–17). At lower temperatures, $\rho_{AHE,nonM}$ is largely suppressed with approaching the forced FM phase. At higher temperatures, on the other hand, $\rho_{AHE,nonM}$ also gradually decreases with elevating temperature, reflecting more randomly oriented spin states.

To discuss possible origins of the observed large AHE, we consider how the local spin correlation with finite spin chirality affects electron conduction in the hopping regime. Electron conduction in this regime is described by phonon-assisted hopping of electrons localized on a site, as schematically shown in Fig. 4B. The electron trajectory skews when they are coupled strongly to the underlying localized moments (see also the Materials and Methods). Figure 4 (C and D) shows typical temperature dependence of σ_{xx} and $\sigma_{AHE,cl.skew}$ calculated assuming constant spin chirality, with comparing to the measured ones in Fig. 4 (E and F). A weak temperature dependence of σ_{xx} characteristic in the hopping conduction is well reproduced in this model (Fig. 4, C and E). On the other hand, the calculation shows that $\sigma_{AHE,cl.skew}$ rapidly increases with elevating temperature (Fig. 4D) and then decreases above $T/\omega_{ph} \sim 5$, while $\sigma_{AHE,nonM}$ in EuAs reaches a maximum at about 70 K (Fig. 4F). This indicates that the local spin chirality in EuAs is gradually reduced by thermal fluctuation above T_N and also suggests future possibility that anomalous Hall angles even exceeding the

present value could be achieved in other semiconductor systems that host finite spin chirality at much higher temperatures.

DISCUSSION

In the hopping conduction regime, to be precise, the extrinsic mechanism cannot be distinguished from the intrinsic one because the band picture of magnetotransport is not preserved anymore. On the other hand, its temperature dependence greatly differs from the one in the intrinsic mechanism. In the spin cluster skew scattering, thermal average of the spin chirality $\langle S_i \cdot (S_j \times S_k) \rangle$, not the spin chirality of averaged spins $\langle S_i \rangle \cdot (\langle S_j \rangle \times \langle S_k \rangle)$ as in the intrinsic mechanism, contributes to the anomalous Hall conductivity, and this remains finite even above the magnetic ordering temperature (19). This is consistent with our observation that in EuAs, the M -nonproportional AHE emerges up to high temperatures much above T_N , while the intrinsic AHE disappears above the magnetic ordering temperature.

It is also instructive to mention that M -nonproportional AHE above the magnetic ordering temperature has been reported for $\text{La}_{1-x}\text{Sr}_x\text{MnO}_3$ (36) and EuTe (41) in the past, which also exhibit CMR in the hopping regime. While this AHE has been also ascribed to thermally fluctuating spins forming local noncoplanar structures near the magnetic ordering temperature (36), their Hall angles were very small due to simple FM or AFM ordering without frustration at the ground state. In EuAs, noncoplanar fluctuation may survive much above the magnetic ordering temperature, largely enhancing the spin cluster skew scattering. In this context, triangular-lattice

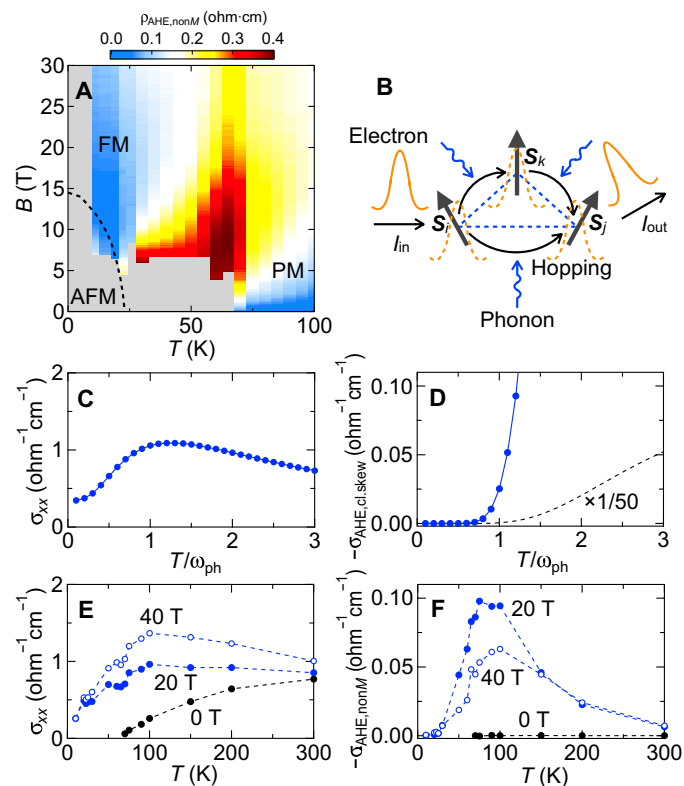


Fig. 4. Large AHE in the hopping regime. (A) Color map of $\rho_{\text{AHE,nonM}}$ on the magnetic phase diagram. ρ_{yx} below about 5 T and 60 K could not be measured because the sample becomes too insulating. (B) Schematic picture of the skew scattering process in the hopping conduction regime, producing AHE proportional to the scalar spin chirality. Temperature dependence of (C) longitudinal conductivity σ_{xx} and (D) M -nonproportional anomalous Hall conductivity originating in the spin cluster skew scattering $-\sigma_{\text{AHE,cl.skew}}$, which is calculated for $t/\omega_{\text{ph}} = 300$ assuming constant spin chirality. (E) σ_{xx} and (F) $\rho_{\text{AHE,nonM}}$ experimentally obtained at typical magnetic fields. Difference between $\sigma_{\text{AHE,cl.skew}}$ and $\rho_{\text{AHE,nonM}}$ at high temperatures is mainly explained by a decrease in spin chirality due to thermal fluctuations in EuAs.

magnetic semiconductors forming magnetic sublattices with finite spin chirality (42) may be promising as further targets.

In summary, we have studied magnetotransport of novel magnetic semiconductor EuAs with large Heisenberg Eu^{2+} spin moments on the distorted triangular lattice. EuAs exhibits CMR even at far higher temperatures than T_N , indicating strong coupling between the localized spins and diluted carriers and also AFM spin fluctuations evolving on the frustrated lattice. In the Hall transport, nonmonotonic AHE with large Hall angles is observed up to high temperatures much above T_N . Considering that the signal appears centered at the paramagnetic phase, skew scattering by multiple spins with finite spin chirality is a possible origin of the large AHE observed in the hopping regime, as also supported by the model calculations of polaron motion on the noncoplanar spin texture. Our findings pave the way for studying magnetic semiconductors hosting topological spin textures. Emergent magnetotransport that originates in low-density charge carriers strongly coupled to short-period noncoplanar spin structures includes large nonmonotonic AHE and its quantization (24, 25), which are expected to be markedly controlled by semiconductor techniques such as electrostatic gating and chemical doping.

MATERIALS AND METHODS

Epitaxial film growth

EuAs films were grown in an EpiQuest RC1100 MBE chamber on single-crystalline (0001) Al_2O_3 substrates. Al_2O_3 has a trigonal structure, and the lattice mismatch between EuAs and Al_2O_3 is only 1.1%, as illustrated in Fig. 1B. The molecular beams were provided from a conventional Knudsen cell containing Eu (3N, Nippon Yttrium Co. Ltd.) and an MBE-Komponenten valved cracker source containing As (7N5, Furukawa Denshi Co. Ltd.), respectively. The reservoir temperature of the cracker source was set to 950°C to sublime arsenic as As_2 . The growth temperature was set to 1000°C , and the beam equivalent pressures, measured by an ionization gauge, were set to 3×10^{-5} Pa for Eu and 1.2×10^{-4} Pa for As_2 during the growth. The film thicknesses were typically designed at 100 nm for structural characterization, 400 nm for magnetotransport measurements, and 1 μm for magnetization measurements and neutron diffraction experiments. The growth rate was about 0.4 $\text{\AA}/\text{s}$.

Magnetotransport measurements

Longitudinal resistivity ρ_{xx} and Hall resistivity ρ_{yx} were measured with a standard four probe method. Nickel and gold electrode was deposited on terminals of the sample for better ohmic contact, and then, SiO_2 capping layer was entirely deposited for preventing oxidation of EuAs. Aluminum wire was connected to the terminals by using an ultrasonic bonding machine, and these connections were reinforced by applying silver paste. Transport measurements up to 56 T were performed using a nondestructive pulsed magnet with a pulse duration of 37 ms at the International MegaGauss Science Laboratory at the Institute for Solid State Physics, The University of Tokyo. Longitudinal resistivity ρ_{xx} below 14 T was also measured using a Quantum Design Physical Properties Measurement System.

Magnetization measurements

Magnetization curves up to 27 T were taken for 1- μm -thick EuAs films using a nondestructive pulsed magnet with a pulse duration of 4 ms at the International MegaGauss Science Laboratory in the Institute for Solid State Physics, The University of Tokyo. Temperature dependence at 0.1 T was measured using a superconducting quantum interference device magnetometer in a Quantum Design Magnetic Property Measurement System.

Neutron diffraction experiments

Unpolarized and polarized neutron scattering experiments were performed at the small- and wide-angle neutron scattering instrument TAIKAN (BL15) in Materials and Life Science Experimental Facility in Japan Proton Accelerator Research Complex. An EuAs film with a thickness of 1 μm was loaded in an aluminum cell with He gas and then installed in a closed-cycle 4He refrigerator and a horizontal field cryomagnet for unpolarized and polarized experiments, respectively. Time-of-flight neutron diffraction patterns were taken using a pulsed incident neutron beam with a wavelength range from 0.7 to 7.7 \AA . For the polarized neutron scattering experiment, the incident neutron beam was spin polarized by a supermirror polarizer. To maintain spin polarization of the incident neutrons, we applied a magnetic field of 0.05 T parallel to the c axis at the sample position. We also used a supermirror to analyze the spin state of the scattered neutrons, in which wavelength was 3.25 \AA when measuring magnetic Bragg reflections in the first Brillouin zone.

The polarization direction of the incident neutrons was set to be parallel or antiparallel to the c axis using a spin flipper. We then measured intensities of the magnetic Bragg reflection for SF and NSF scattering processes. The beam polarization for neutrons with the wavelength of 3.25 Å was 0.92. The SF and NSF intensities shown in Fig. 2E have been corrected taking into account the imperfection of the beam polarization.

Theoretical calculation of hall current

The Hall conductivity was calculated according to the method developed for polaron motion (26, 43). Later, this method was used to evaluate the spin chirality-related Hall effect in the CMR manganites (36). Following these studies, we consider a double-exchange model coupled to phonons

$$H = \sum_{ij} t_{ij} c_i^\dagger c_j + \sum_q \omega_q a_q^\dagger a_q + \sum_{iq} M_q e^{iq \cdot r_i} c_i^\dagger c_i (a_q + a_{-q}^\dagger) - \sum_i e \mathbf{E} \cdot \mathbf{r}_i c_i^\dagger c_i \quad (4)$$

Here, c_i (c_i^\dagger) is the annihilation (creation) operator of an electron at site i , a_q (a_q^\dagger) is the annihilation (creation) operator for phonons, M_q is the electron-phonon coupling, and $e \mathbf{E} \cdot \mathbf{r}_i$ is the electric potential due to the external electric field $\mathbf{E} = (E, 0)$. Here, the electrons are effectively spinless, as the electron spins are polarized along the underlying magnetic texture. Instead, the effect of magnetic correlation appears in the hopping integral $t_{ij}(\mathbf{S}_i, \mathbf{S}_j) = \cos(\theta_i/2) \cos(\theta_j/2) + \sin(\theta_i/2) \sin(\theta_j/2) e^{i(\phi_j - \phi_i)}$ (34, 35). In what follows, we assume only nearest-neighbor hopping, and the phonons are Einstein phonons, i.e., $M_q = M$ and $\omega_q = \omega_{\text{ph}}$.

In the polaron theory, the leading order in electron conduction appears from the second order in hopping (43)

$$J_{i \rightarrow j} = -e \frac{|t_{ij}|^2 E_x (r_j^x - r_i^x)}{\hbar \omega_{\text{ph}}^2} 2F_0 \left(\frac{M}{\omega_{\text{ph}}}, \frac{V_0}{\omega_{\text{ph}}} \right) \quad (5)$$

where

$$F_0(x, y) = \int_{-\infty}^{\infty} d\tau' i\tau' e^{-y^2 \tilde{\phi}(\tau) - x^2 \tau^2} \quad (6)$$

$$\tilde{\phi}(\tau) = 2[1 - \cos(\tau)][2n_{\text{ph}} \left(\frac{k_{\text{B}} T}{\omega_{\text{ph}}} \right) + 1] + i \sin(\tau) \quad (7)$$

$$n_{\text{ph}}(x) = \frac{1}{\exp(1/x) - 1} \quad (8)$$

This term gives the longitudinal current

$$J_x = \frac{1 + \langle \mathbf{S}_i \cdot \mathbf{S}_j \rangle \sqrt{3} e^2 n t^2 E}{2 \hbar \omega_{\text{ph}}^2} F_0 \left(\frac{M}{\omega_{\text{ph}}}, \frac{V_0}{\omega_{\text{ph}}} \right) \quad (9)$$

when the electron field is along the x axis. Here, $\langle \mathbf{S}_i \cdot \mathbf{S}_j \rangle$ is the thermal average of the dot product of spins on i and j sites.

The Hall current appears from the cubic order in hopping. The electric current flowing from site i to j reads

$$J_{i \rightarrow j} = \frac{4eE(r_j^x - r_i^x)}{\hbar} \sum_m \frac{\text{Re}(t_{ij} t_{jm} t_{mi})}{\omega_{\text{ph}}^3} + \sum_m \frac{2eE(2r_m^x - r_i^x - r_j^x)}{\hbar} \frac{\text{Im}(t_{ij} t_{jm} t_{mi})}{\omega_{\text{ph}}^3} \text{Im} \left[F_2 \left(\frac{M}{\omega_{\text{ph}}}, \frac{V_0}{\omega_{\text{ph}}} \right) \right] \quad (10)$$

with V_0 , where

$$F_1(x, y) = \int_{-\infty}^{\infty} d\tau \int_{-\infty}^{\infty} d\tau' \tau e^{-x^2 \tilde{\phi}^{(3)}(\tau, 0, \tau) - y^2 (\tau^2 + \tau'^2 - \tau\tau')} \quad (11)$$

$$F_2(x, y) = \int_{-\infty}^{\infty} d\tau \int_{-\infty}^{\infty} d\tau' \tau' e^{-x^2 \tilde{\phi}^{(3)}(\tau, 0, \tau) - y^2 (\tau^2 + \tau'^2 - \tau\tau')} \quad (12)$$

and

$$\tilde{\phi}^{(3)}(\tau_1, \tau_2, \tau_3) = (3 - e^{i(\tau_2 - \tau_1)} - e^{i(\tau_3 - \tau_1)} - e^{i(\tau_3 - \tau_2)}) \left[n_{\text{ph}} \left(\frac{k_{\text{B}} T}{\omega_{\text{ph}}} \right) + 1 \right] + (3 - e^{-i(\tau_2 - \tau_1)} - e^{-i(\tau_3 - \tau_1)} - e^{-i(\tau_3 - \tau_2)}) n_{\text{ph}} \left(\frac{k_{\text{B}} T}{\omega_{\text{ph}}} \right) \quad (13)$$

Using the above formula for the current, the transverse current reads

$$J_y = -\frac{3\sqrt{3} e^2 n t^3 E}{2 \hbar \omega_{\text{ph}}^3} (\chi_u + \chi_d) \text{Im} \left[F_2 \left(\frac{M}{\omega_{\text{ph}}}, \frac{V_0}{\omega_{\text{ph}}} \right) \right] \quad (14)$$

where χ_u (χ_d) is the thermal average of the scalar spin chirality $\mathbf{S}_i \cdot (\mathbf{S}_j \times \mathbf{S}_k)$ for the upward (downward) triangles. Here, the sites i, j , and k are in counterclockwise order. The result implies that a finite Hall current forms when $\chi_u \neq -\chi_d$. The imbalance of chirality generally occurs when the upward and downward triangles are inequivalent, such as in the trimerized case.

SUPPLEMENTARY MATERIALS

Supplementary material for this article is available at <https://science.org/doi/10.1126/sciadv.abl5381>

REFERENCES AND NOTES

- N. Nagaosa, J. Sinova, S. Onoda, A. H. MacDonald, N. P. Ong, Anomalous Hall effect. *Rev. Mod. Phys.* **82**, 1539–1592 (2010).
- R. Karplus, J. M. Luttinger, Hall effect in ferromagnetics. *Phys. Rev.* **95**, 1154–1160 (1954).
- J. Smit, The spontaneous hall effect in ferromagnetics II. *Phys. Ther.* **24**, 39–51 (1958).
- L. Berger, Side-jump mechanism for the Hall effect of ferromagnets. *Phys. Rev. B* **2**, 4559–4566 (1970).
- J. Ye, Y. B. Kim, A. J. Millis, B. I. Shraiman, P. Majumdar, Z. Tešanović, Berry phase theory of the anomalous Hall effect: Application to colossal magnetoresistance manganites. *Phys. Rev. Lett.* **83**, 3737–3740 (1999).
- K. Ohgushi, S. Murakami, N. Nagaosa, Spin anisotropy and quantum Hall effect in the *kagomé* lattice: Chiral spin state based on a ferromagnet. *Phys. Rev. B* **62**, R6065–R6068 (2000).
- G. Tatara, H. Kawamura, Chirality-driven anomalous Hall effect in weak coupling regime. *J. Phys. Soc. Jpn.* **71**, 2613–2616 (2002).
- Y. Taguchi, Y. Oohara, H. Yoshizawa, N. Nagaosa, Y. Tokura, Spin chirality, Berry phase, and anomalous Hall effect in a frustrated ferromagnet. *Science* **291**, 2573–2576 (2001).
- Z. Fang, N. Nagaosa, K. S. Takahashi, A. Asamitsu, R. Mathieu, T. Ogasawara, H. Yamada, M. Kawasaki, Y. Tokura, K. Terakura, The anomalous Hall effect and magnetic monopoles in momentum space. *Science* **302**, 92–95 (2003).
- M. Lee, W. Kang, Y. Onose, Y. Tokura, N. P. Ong, Unusual Hall effect anomaly in MnSi under pressure. *Phys. Rev. Lett.* **102**, 186601 (2009).
- A. Neubauer, C. Pfleiderer, B. Binz, A. Rosch, R. Ritz, P. G. Niklowitz, P. Böni, Topological Hall effect in the A phase of MnSi. *Phys. Rev. Lett.* **102**, 186602 (2009).
- S. Nakatsuji, N. Kiyohara, T. Higo, Large anomalous Hall effect in a non-collinear antiferromagnet at room temperature. *Nature* **527**, 212–215 (2015).
- E. Liu, Y. Sun, N. Kumar, L. Muechler, A. Sun, L. Jiao, S.-Y. Yang, D. Liu, A. Liang, Q. Xu, J. Kroder, F. Süß, H. Borrmann, C. Shekhar, Z. Wang, C. Xi, W. Wang, W. Schnelle, S. Wirth, Y. Chen, S. T. B. Goennenwein, C. Felser, Giant anomalous Hall effect in a ferromagnetic kagome-lattice semimetal. *Nat. Phys.* **14**, 1125–1131 (2018).
- T. Suzuki, R. Chisnell, A. Devarakonda, Y.-T. Liu, W. Feng, D. Xiao, J. W. Lynn, J. G. Checkelsky, Large anomalous Hall effect in a half-Heusler antiferromagnet. *Nat. Phys.* **12**, 1119–1123 (2016).
- L. Ye, M. Kang, J. Liu, F. von Cube, C. R. Wicker, T. Suzuki, C. Jozwiak, A. Bostwick, E. Rotenberg, D. C. Bell, L. Fu, R. Comin, J. G. Checkelsky, Massive Dirac fermions in a ferromagnetic kagome metal. *Nature* **555**, 638–642 (2018).
- K. Kim, J. Seo, E. Lee, K.-T. Ko, B. S. Kim, B. G. Jang, J. M. Ok, J. Lee, Y. J. Jo, W. Kang, J. H. Shim, C. Kim, H. W. Yeom, B. I. Min, B.-J. Yang, J. S. Kim, Large anomalous Hall current

- induced by topological nodal lines in a ferromagnetic van der Waals semimetal. *Nat. Mater.* **17**, 794–799 (2018).
17. A. Sakai, Y. P. Mizuta, A. A. Nugroho, R. Sihombing, T. Koretsune, M. Suzuki, N. Takemori, R. Ishii, D. Nishio-Hamane, R. Arita, P. Goswami, S. Nakatsuji, Giant anomalous Nernst effect and quantum-critical scaling in a ferromagnetic semimetal. *Nat. Phys.* **14**, 1119–1124 (2018).
 18. A. A. Burkov, Anomalous Hall effect in Weyl metals. *Phys. Rev. Lett.* **113**, 187202 (2014).
 19. H. Ishizuka, N. Nagaosa, Spin chirality induced skew scattering and anomalous Hall effect in chiral magnets. *Sci. Adv.* **4**, eaap9962 (2018).
 20. H. Ishizuka, N. Nagaosa, Large anomalous Hall effect and spin Hall effect by spin-cluster scattering in the strong-coupling limit. *Phys. Rev. B* **103**, 235148 (2021).
 21. N. Kanazawa, Y. Onose, T. Arima, D. Okuyama, K. Ohoyama, S. Wakimoto, K. Kakurai, S. Ishiwata, Y. Tokura, Large topological Hall effect in a short-period helimagnet MnGe. *Phys. Rev. Lett.* **106**, 156603 (2011).
 22. Y. Fujishiro, N. Kanazawa, R. Kurihara, H. Ishizuka, T. Hori, F. S. Yasin, X. Yu, A. Tsukazaki, M. Ichikawa, M. Kawasaki, N. Nagaosa, M. Tokunaga, Y. Tokura, Giant anomalous Hall effect from spin-chirality scattering in a chiral magnet. *Nat. Commun.* **12**, 317 (2021).
 23. S.-Y. Yang, Y. Wang, B. R. Ortiz, D. Liu, J. Gayles, E. Derunova, R. Gonzalez-Hernandez, L. Smejkal, Y. Chen, S. S. P. Parkin, S. D. Wilson, E. S. Toberer, T. McQueen, M. N. Ali, Giant, unconventional anomalous Hall effect in the metallic frustrated magnet candidate, KV_3Sb_5 . *Sci. Adv.* **6**, eaabb6003 (2020).
 24. Z. Qiao, W. Ren, H. Chen, L. Bellaiche, Z. Zhang, A. H. MacDonald, Q. Niu, Quantum anomalous Hall effect in graphene proximity coupled to an antiferromagnetic insulator. *Phys. Rev. Lett.* **112**, 116404 (2014).
 25. K. Hamamoto, M. Ezawa, N. Nagaosa, Quantized topological Hall effect in skyrmion crystal. *Phys. Rev. B* **92**, 115417 (2015).
 26. T. Holstein, Hall effect in impurity conduction. *Phys. Rev.* **124**, 1329–1347 (1961).
 27. A. A. Burkov, L. Balents, Anomalous Hall effect in ferromagnetic semiconductors in the hopping transport regime. *Phys. Rev. Lett.* **91**, 057202 (2003).
 28. X.-J. Liu, X. Liu, J. Sinova, Scaling of the anomalous Hall effect in the insulating regime. *Phys. Rev. B* **84**, 165304 (2011).
 29. S. Ono, F. L. Hui, J. G. Despault, L. D. Calvert, J. B. Taylor, Rare-Earth pnictides: The arsenic-rich europium arsenide's. *J. Less Common Met.* **25**, 287–294 (1971).
 30. A. Iandelli, E. Franceschi, On the crystal structure of the compounds CaP , SrP , $CaAs$, $SrAs$ and $EuAs$. *J. Less Common Met.* **30**, 211–216 (1973).
 31. B. Y. Wang, E. J. Gabe, L. D. Calvert, J. B. Taylor, Europium–arsenic Eu_2As_2 : A single-crystal structure refinement. *Acta Crystallogr.* **B33**, 131–133 (1977).
 32. C.-G. Duan, R. F. Sabirianov, W. N. Mei, P. A. Dowben, S. S. Jaswal, E. Y. Tsymlal, Electronic, magnetic and transport properties of rare-earth monopnictides. *J. Phys. Condens. Matter* **19**, 315220 (2007).
 33. L. Petit, R. Tyer, Z. Szotek, W. M. Temmerman, A. Svane, Rare earth monopnictides and monochalcogenides from first principles: Towards an electronic phase diagram of strongly correlated materials. *New J. Phys.* **12**, 113041 (2010).
 34. C. Zener, Interaction between the d -shells in the transition metals. II. Ferromagnetic compounds of manganese with perovskite structure. *Phys. Rev.* **82**, 403–405 (1951).
 35. P. W. Anderson, H. Hasegawa, Considerations on double exchange. *Phys. Rev.* **100**, 675–681 (1955).
 36. Y. Lyanda-Geller, S. H. Chun, M. B. Salamon, P. M. Goldbart, P. D. Han, Y. Tomioka, A. Asamitsu, Y. Tokura, Charge transport in manganites: Hopping conduction, the anomalous Hall effect, and universal scaling. *Phys. Rev. B* **63**, 184426 (2001).
 37. Y. Tokura, Y. Tomioka, Colossal magnetoresistive manganites. *J. Magn. Magn. Mater.* **200**, 1–23 (1999).
 38. P. Matl, N. P. Ong, Y. F. Yan, Y. Q. Li, D. Studebaker, T. Baum, G. Doubinina, Hall effect of the colossal magnetoresistance manganite $La_{1-x}Ca_xMnO_3$. *Phys. Rev. B* **57**, 10248–10251 (1998).
 39. Y. Shapira, S. Foner, T. B. Reed, EuO. I. Resistivity and Hall effect in fields up to 150 kOe. *Phys. Rev. B* **8**, 2299–2315 (1973).
 40. H. Sakurai, T. Kolodiaznyh, Y. Michiue, E. Takayama-Muromachi, Y. Tanabe, H. Kikuchi, Unconventional colossal magnetoresistance in sodium chromium oxide with a mixed-valence state. *Angew. Chem. Int. Ed.* **51**, 6653–6656 (2012).
 41. Y. Shapira, S. Foner, N. F. Oliveira Jr., EuTe. II. Resistivity and Hall effect. *Phys. Rev. B* **5**, 2647–2657 (1972).
 42. I. Martin, C. D. Batista, Itinerant electron-driven chiral magnetic ordering and spontaneous quantum Hall effect in triangular lattice models. *Phys. Rev. Lett.* **101**, 156402 (2008).
 43. T. Holstein, Studies of polaron motion: Part II. The “small” polaron. *Ann. Phys.* **8**, 343–389 (1959).
 44. J. A. Mundy, D. Hodash, A. Melville, R. Held, T. Mairoser, D. A. Muller, L. F. Kourkoutis, A. Schmelh, D. G. Schlom, Hetero-epitaxial EuO interfaces studied by analytic electron microscopy. *Appl. Phys. Lett.* **104**, 091601 (2014).
 45. S. Onoda, N. Sugimoto, N. Nagaosa, Quantum transport theory of anomalous electric, thermoelectric, and thermal Hall effects in ferromagnets. *Phys. Rev. B* **77**, 165103 (2008).

Acknowledgments: We acknowledge fruitful discussions with Y. Tokura, Y. Taguchi, N. Kanazawa, M. Hirschberger, K. Ishizaka, M. Sakano, S. Yoshida, and Y. Ohigashi. Unpolarized/polarized neutron scattering experiments were performed at Materials and Life Science Experimental Facility (MLF) in Japan Proton Accelerator Research Complex (J-PARC) (proposal nos. 2017L0701 and 2019C0006). **Funding:** This work was supported by JST PRESTO grant no. JPMJPR18L2 and CREST grant no. JPMJCR16F1, Japan; by Grant-in-Aids for Scientific Research (B) nos. JP18H01866, JP19H01856, JP17H02815, and JP21H01804 from MEXT, Japan; and by Inamori Foundation, Japan. **Author contributions:** M.U. and M.Ka. designed the experiments. M.U., S.S., and Y.N. grew films and performed transport measurements with R.K. and M.T., and magnetization measurements with M.Kr. and A.M. T.N. performed neutron scattering experiments with K.O., T.M., and T.-h.A. H.I. and N.N. performed model calculation of the anomalous Hall conductivity. M.S.B. performed first principles band structure calculations. M.U. and S.S. analyzed the data and wrote the manuscript with input from all authors. T.-h.A. and N.N. jointly discussed the results. M.U. and M.Ka. conceived the project. All authors have approved the final version of the manuscript. **Competing interests:** The authors declare that they have no competing interests. **Data and materials availability:** All data needed to evaluate the conclusions in the paper are present in the paper and/or the Supplementary Materials.

Submitted 20 July 2021

Accepted 3 November 2021

Published 22 December 2021

10.1126/sciadv.abl5381